# Imaging Strain-Localized Single-Photon Emitters in Layered GaSe Below the Diffraction Limit

Weijun Luo,<sup>1</sup> Benjamin J. Lawrie,<sup>2,3\*</sup> Alexander A. Puretzky,<sup>2\*</sup> Qishuo Tan,<sup>1</sup> Hongze Gao,<sup>1</sup> David B. Lingerfelt,<sup>2</sup> Gage Eichman,<sup>2</sup> Edward Mcgee,<sup>4</sup> Anna K. Swan,<sup>4,5</sup> Liangbo Liang,<sup>2</sup> Xi Ling<sup>1,5,6\*</sup>

\*Correspondence: xiling@bu.edu; lawriebj@ornl.gov; puretzkya@ornl.gov

KEYWORDS: Single photon emission, strain engineering, cathodoluminescence, GaSe

This manuscript has been authored in part by UT-Battelle, LLC, under contract DE-AC05-00OR22725 with the US Department of Energy (DOE). The US government retains and the publisher, by accepting the article for publication, acknowledges that the US government retains a nonexclusive, paid-up, irrevocable, worldwide license to publish or reproduce the published form of this manuscript, or allow others to do so, for US government purposes. DOE will provide public access to these results of federally sponsored research in accordance with the DOE Public Access Plan (<a href="http://energy.gov/downloads/doe-public-access-plan">http://energy.gov/downloads/doe-public-access-plan</a>).

<sup>&</sup>lt;sup>1</sup> Department of Chemistry, Boston University, Boston, MA 02215, United States

<sup>&</sup>lt;sup>2</sup>Center for Nanophase Materials Sciences, Oak Ridge National Laboratory, Oak Ridge, TN 37831, United States

<sup>&</sup>lt;sup>3</sup> Materials Science and Technology Division, Oak Ridge National Laboratory, Oak Ridge, TN 37831, United States

<sup>&</sup>lt;sup>4</sup> Department of Electrical Engineering, Boston University, Boston, MA 02215, United States

<sup>&</sup>lt;sup>5</sup> The Photonics Center, Boston University, Boston, MA 02215, United States

<sup>&</sup>lt;sup>6</sup> Division of Materials Science and Engineering, Boston University, Boston, MA 02215, United States

#### **Abstract**

Nanoscale strain control of exciton funneling is an increasingly critical tool for the scalable production of single photon emitters (SPEs) in two-dimensional materials. However, conventional far-field optical microscopies remain constrained in spatial resolution by the diffraction limit and thus can only provide a limited description of nanoscale strain localization of SPEs. Here, we quantify the effects of nanoscale heterogeneous strain on the energy and brightness of GaSe SPEs on nanopillars with correlative cathodoluminescence, photoluminescence, and atomic force microscopies supported by density functional theory simulations. We report the strain-localized SPEs have a broad range of emission wavelengths from 620 nm to 900 nm. We reveal substantial strain-controlled SPE wavelength tunability over a ~ 100 nm spectral range and two orders of magnitude enhancement in the SPE brightness at the pillar center due to Type-I exciton funneling. In addition, we show that radiative biexciton cascade processes contribute to the observed CL photon superbunching. Also, the GaSe SPEs show excellent stability where their properties remain unchanged after electron beam exposure. We anticipate this comprehensive study on the nanoscale strain control of two-dimensional SPEs will provide key insights to guide the development of truly deterministic quantum photonics.

KEYWORDS: 2D materials, gallium selenide, strain engineering, cathodoluminescence, single photon emission, exciton funneling

Over the past decade, the idea of using nanoscale strain gradients to funnel energy into "artificial atoms" has generated substantial excitement<sup>1</sup>. Strain manipulation of electronic band energies and optical bandgaps in flexible two-dimensional (2D) layered materials has enabled wide tunability of exciton binding energies and transport dynamics<sup>2</sup>. For instance, excitons in monolayer transition metal dichalcogenide (TMDC) MoS<sub>2</sub> experience a redshift of 0.09 eV under a 2.5% localized uniaxial tensile strain<sup>3</sup>; under biaxial tensile strain, they exhibit a linear redshift rate of 0.11 eV/%<sup>4,5</sup>. In addition, dynamic exciton funneling induced by AFM indentation in monolayer WS<sub>2</sub> has resulted in strain-dependent exciton-to-trion conversion. A similar study on WSe<sub>2</sub> demonstrated exciton funneling with a 12 meV redshift at ~ 3% biaxial tensile strain induced by indentation<sup>6</sup>.

The interest in exciton funneling has been further stimulated by the discovery of single photon emitters (SPEs) associated with defects and strain-confined excitons in 2D materials such as layered hBN<sup>7–9</sup> and monolayer TMDCs (i.e., WSe<sub>2</sub>)<sup>10–12</sup>. Specifically, exciton funneling by periodically patterned nano-stressors has emerged as a powerful way to generate deterministic SPEs in monolayer TMDCs<sup>13–16</sup> with controlled position, wavelength, purity, and brightness for widespread applications in quantum information science.

Nonetheless, capturing fine details of exciton funneling with diffraction-limited far-field optical probes remains a critical challenge in studies of SPEs in 2D materials. Exciton diffusion lengths in unstrained monolayers  $^{17-19}$  have been reported to be less than 1  $\mu$ m, and they can be substantially smaller (i.e., < 200 nm) when exciton funneling is induced by nanoscale strain  $^{14,20}$ . Near-field characterization tools with spatial resolution below the diffraction limit are increasingly needed to understand these effects. For example, cathodoluminescence (CL) $^{21-26}$  microscopy has been used to study defect-related SPEs in 2D hBN. Tip-enhanced PL $^{27-29}$  and scanning tunneling luminescence  $^{30}$  microscopies have been used to study localized emitters in quantum dots, carbon nanotubes, and monolayer WSe2. Compared to the other techniques, CL microscopy provides an approach to performing non-contact measurements at low temperatures with exceptional selectivity in identifying specific areas of interest and compatibility with photon antibunching measurements. However, previous work on CL study of SPEs in monolayer TMDCs showed that the electron beam often induced damage in these materials and was detrimental to the SPE performance. Indeed, monolayer TMDCs must be encapsulated with hBN $^{31-33}$  for CL imaging,

which introduces additional challenges because of the potential for electron beam-induced excitations in each layer of the stack<sup>34</sup>. For the reasons mentioned above, using CL to study the SPEs in 2D materials has been hindered.

The study of GaSe as an SPE host is in its infancy.<sup>35,36</sup> In our recent work, we demonstrated a deterministic generation of SPEs in multilayer GaSe through strain localization provided by lithographically patterned nanopillar arrays<sup>16</sup>. Herein, we investigate the SPE characteristics of locally strained multilayer GaSe using CL microscopy supported by atomic force microscopy (AFM), photoluminescence (PL), and photon antibunching measurements. Due to the robustness of the multilayer GaSe under the electron beam, comprehensive information about how nanoscale strain affects the formation, wavelength, and intensity of GaSe SPEs is obtained. First, we show a broad range of emission wavelengths from 620 nm to 900 nm of the strain-localized SPEs. With correlative CL and AFM measurements, we reveal that the strain plays a vital role in controlling the energy and brightness of localized GaSe emitters by observing a continuous redshift in emission wavelengths from 680 nm to 780 nm and enhancement of emitter brightness by two orders of magnitude with increasing strain. The spectral tuning is explained by a strain-induced redshift of the bandgap modeled with density functional theory (DFT) simulations. Moreover, strain-induced decrease in conduction band minimum (CBM) and increase in valence band maximum (VBM) are observed, leading to the exciton funneling effect and then the enhancement of the emission intensity. Photon bunching and antibunching of the same emitters on pillars are observed from CL and PL measurements, respectively. No beam-induced degradation of the photophysical properties of the emitters during the CL and PL measurements are observed, further showcasing the excellent stability of the GaSe SPEs. This research provides key insights on the origin, property, and manipulation of SPEs in multilayer GaSe, shines light on the potential for engineering SPEs in 2D materials using strain, and lays a crucial foundation for developing 2D quantum photonic devices.

#### **Results and Discussion**

## Hyperspectral CL mapping of multilayer GaSe on SiO2 nanopillars

To introduce biaxial tensile strain to GaSe, we stacked  $\varepsilon$ -type GaSe flakes onto the patterned SiO<sub>2</sub> nanopillar arrays using the dry-transfer method as described in our previous work<sup>16</sup>. As illustrated in Figure 1a, the flake pins to the upper edges of each nanopillar and forms a quasi-circular biaxially tented region. This circular tent forms a strain field where the biaxial tensile strain starts at zero outside the circle and then increases continuously until maximizing at the tent apex. Figure 1b shows an SEM image of a thick GaSe flake (thickness ~ 150 nm) tented on SiO<sub>2</sub> nanopillar arrays. Hyperspectral CL images are acquired for a variety of nanopillars and demonstrate a wide emission wavelength distribution spanning ~590 nm (~2.10 eV) to ~900 nm (~1.38 eV). Note GaSe is an indirect semiconductor with a small energy difference between its direct bandgap (2.07 eV) and indirect bandgap (2.03 eV), resulting in the observed broadband direct, indirect, and bound exciton emissions between ~590 nm (~2.10 eV) and ~620 nm (~2.0 eV)<sup>37,38</sup>. Figures 1c and 1d highlight the large-area CL response across the inset optical image in Figure 1b. Figure 1c illustrates the integrated CL intensity for wavelengths between 590 nm (~ 2.10 eV) and ~ 620 nm (~ 2.0 eV), corresponding to the band edge emission of GaSe; in this band, most of the CL is observed around the circumference of the tents, with minimal CL observed at the center of the pillars or in the unstrained areas between pillars. Figure 1d illustrates the integrated CL intensities between 650 and 900 nm, which are below the indirect bandgap of unstrained GaSe. These subbandgap emissions localize near the centers of the tents. The full hyperspectral CL mapping across these pillars is also visualized<sup>39</sup>. A statistical description of the emission wavelengths of the strongest emission band in each CL spectrum is summarized and shown in Supplementary Figure S1a.

While the spectrum image shown in **Figure 1** provides a global picture of the effect of strain on excitons in GaSe, it is limited to a 180 nm spatial resolution because of the 100 ms dwell time required to acquire a spectrum at each pixel and the size of the composite image. In the following sections, we investigate the strain-controlled emission properties with higher spatial resolution and reduced field of view.

### Hyperspectral CL line scan and AFM measurements of multilayer GaSe on SiO2 nanopillars

In order to better understand the effects of nanoscale strain gradients on excitons in GaSe, a high-resolution CL line scan across two pillars with a spatial resolution of 20 nm was performed on a 70-nm-thick flake shown in **Figure 2a**. **Figure 2b** shows an AFM height profile across pillars A and B. The fabricated pillars have conical frustum geometries as a result of the reactive ion etching process, and the full width at half maximum (FWHM) of pillars A and B are 450 nm and 410 nm, respectively. When GaSe is transferred on the pillars, the average height of both tents is  $\sim 1.00$  nm while the average FWHM is  $\sim 1.1 \ \mu m$ . The peak-to-peak distance of the two tents is  $\sim 2.6 \ \mu m$ .

The dashed white arrow in the SEM image in the left panel of Figure 2c illustrates the CL linescan path from the region slightly above tent A (position 1), across the apex of tent A (position 2), the flat region between tent A and B (position 3), and the apex of tent B (position 4), to the flat region below tent B (position 5). The right panel of Figure 2c shows the position-dependent CL spectra acquired by the CL line scan. As the electron beam approaches the apex of tents A and B, the broad band-edge emission between 590 nm (~ 2.10 eV) and 620 nm (~2.0 eV) experiences a slight redshift (up to ~20 nm), and its intensity decreases gradually. This observation of decreasing indirect-exciton emission intensity with increasing strain is common in 2D layered materials<sup>40,41</sup>. At the tent apex, the band edge emission almost vanishes. Meanwhile, sub-bandgap CL bands near 700 nm (~1.77 eV) and 750 nm (~1.65 eV) are strongly enhanced and redshifted with increasing strain. We attribute these bands to the localized excitons that are associated with trap states in GaSe<sup>35,37,38,42,43</sup>. In addition, as shown in Figure S2a, the sub-bandgap CL enhancement was quantified through the position-dependent integrated CL intensity ratio  $\frac{I_{XS}}{I_{Ea}}$ , which is the ratio of the integrated sub-bandgap CL intensity ( $I_{X_S}$ , between 650 nm and 800 nm) over the band-edge CL intensity ( $I_{E_g}$ , between 590 nm and 650 nm). The sub-bandgap CL is two orders ( $\frac{I_{X_S}}{I_{E_g}} = 184$ ) and one order  $(\frac{I_{X_S}}{I_{E_B}} = 16)$  of magnitude stronger than the band-edge CL on tents A and B. The CL results for tents A and B show strong consistency, with the only exception being the sub-bandgap emission intensity. This suggests that the sub-bandgap CL bands on each pillar arise from the same type of defect-induced trap states. However, the difference in radiative efficiency between tents A and B could be attributed to inhomogeneous defects with varying carrier concentrations. This

variation was the primary reason for the differences in the intensity of single photon emitters across sites in 2D hBN and WSe<sub>2</sub><sup>15,44,45</sup>.

CL bands on the pillar apexes are significantly redshifted (up to ~ 100 nm). Similar strain-induced redshifts and enhancement of emission intensities have been reported for SPEs in strained monolayer WSe<sub>2</sub> <sup>13,14</sup>. The increasing strain from the pillar edge to pillar apex results in a continuous decrease in the bandgap and tuning of the bandgap across randomly distributed trap states, resulting in significantly improved radiative efficiency<sup>14,15</sup>. Moreover, a previous study on PL emission of unstrained GaSe flakes<sup>46</sup> suggests that the prevalence of non-radiative decay pathways due to surface traps causes the low quantum efficiency of the sub-bandgap luminescence.

Five CL spectra collected at positions 1-5 are presented in **Figure 2d**: spectra 1 and 3 (collected at the edges of tents A and B) show weak band edge CL centered at 610 nm ( $\sim 2.03$  eV) and even weaker sub-bandgap CL bands near 700 nm (1.77 eV); spectra 2 and 4 are collected at the apexes of tents A and B, where the sub-bandgap emission at  $\sim 780$  nm dominates the CL spectrum; spectrum 5 is collected away from tents A and B and only shows weak band-edge CL centered at 605 nm (2.05 eV) and 610 nm ( $\sim 2.03$  eV) without any sub-bandgap CL observed.

## Correlative microscopy and strain simulations of a single tent

To understand the spatial correlation between nanoscale biaxial strain and excitonic luminescence in a quantitative fashion, we perform hyperspectral CL mapping of a single tent with ~40 nm spatial resolution and reveal its correlation with the biaxial strain within that tent based on Landau continuum theory<sup>20,47</sup>. **Figure 3a** shows an SEM image of tent A (highlighted in the optical image of **Figure 2a)**, where the dark square indicates the CL mapping area. No obvious beam-induced damage was observed within this area, but a higher pixel density was used within the CL mapping area, causing the change in contrast. **Figure 3b** shows an AFM image of the same area. The area in the dashed circle is the tent area, which is ~ 1.3  $\mu$ m in diameter. **Figure 3c** illustrates the simulated strain divided into three regions by the two dashed circles: 1. high-strain area (1.0% - 2.6%); 2. low-strain area (0% - 1.0%); 3. strain-free area (0%). The strain-free region is more than ~ 1.4  $\mu$ m away from the center of tent A; the high-strain area (1.0% - 2.6%) is less than ~ 0.6  $\mu$ m

from the center of tent A; the low-strain area lies in the annulus between the strain-free and highstrain areas.

This delineation of distinct strain regions is enabled by the analysis of the principal components of the spectrum image via non-negative matrix factorization (NMF). NMF is a powerful linear algebra algorithm for multivariate analysis that has been widely used for modeling spatial and temporal variation and evolution of principal spectral components in spectroscopic studies, including fluorescence images<sup>48,49</sup> and CL microscopy<sup>24,50</sup>. NMF treats a spectrum image as a product matrix M of two matrices W (weight) and P (principal component):  $M = W \times P$ . Therefore, a CL hyperspectral map can be interpreted as the spatially weighted sum of its spectral components (emission wavelengths). For the CL spectrum image of tent A, ten principal emission lines are identified (see more details in Table S1 in Supplementary information). Here, because initial analysis indicated no strong correlations between distinct spectral lines, the ten spectral components from the CL mapping of pillar A were fit to Voigt functions and used as priors for NMF analysis (see more details in Section 2 of Supplementary Information). The spatial distribution of the three most prominent components centered at 610 nm, 703 nm, and 760 nm are illustrated in Figure 3d-f. Other spectral lines with lower intensity are described in supplementary Figure S4. Figure 3d shows that the band-edge emission centered at 610 nm emerges in the lowstrain area between the outer and inner dashed circles. In contrast, sub-bandgap CL at 703 nm and 760 nm is observed primarily in the high-strain area inside the inner circle (Figures 3e and 3f). The intensities of the sub-bandgap CL bands in the high-strain area are one order of magnitude stronger than the band edge CL observed in the low-strain area, which is supported by the mapping results of the position-dependent integrated CL intensity ratio  $\frac{I_{X_S}}{I_{E_R}}$  shown in **Figure S2b**.

Similar analyses for all ten CL spectral components are shown in supplementary **Figure S4**, clearly illustrating the CL redshift with increasing strain. We also performed PL mapping and NMF analysis over pillar A with an incident power density of  $15 \text{ nW}/\mu m^2$ . The result is summarized in **Figures S5**, **S6**, and **S7** and is roughly consistent with the CL results despite the relatively coarse spatial resolution of PL microscopy. In short, the CL mapping results clearly show a strong correlation between the strain and the emission in GaSe, where the band edge emission and subbandgap emission wavelengths can be tuned in a large range from 590 nm (2.10 eV) to 630 nm

(1.97 eV) and 680 nm (1.82 eV) to 780 nm (1.59 eV), respectively. Moreover, the tensile strain-controlled redshift rate of sub-bandgap emission energy is calculated as ~100 meV/%, which is much larger than that of 51 meV/% for strain-localized WSe<sub>2</sub> SPEs<sup>14</sup>.

## DFT calculations of band structures of biaxially tensile-strained GaSe

To better understand the origins of the strain-induced redshifts and changes in the intensities of both band-edge and sub-bandgap CL, we simulate the band structure of bulk GaSe under the biaxial tensile strain of 0% to 6% with DFT using the PBE functional. As shown in **Figure 4a**, under increasing biaxial tensile strain, the conduction band energies continuously decrease while the valence band energies increase (Supplementary Figure **S10a**), resulting in a bandgap redshift rate of -0.16 eV/% (**Figure 4b**). While DFT calculations with PBE functionals usually underestimate bandgaps, our focus here is on the change in bandgap with increasing strain rather than on quantitative models of the actual bandgap. Thus, the observed redshift of band-edge CL is consistent with the strain-induced bandgap redshift from the simulation results.

GaSe retains its indirect gap across the full range of modeled strain; no strain-induced indirect-to-direct transitions are observed from the simulation results. However, the DFT model does show that the momentum difference between the CBM and VBM for the strained GaSe is larger than that of unstrained GaSe (Supplementary **Figure S10b**), which might explain the strain-induced decrease in band edge CL intensity. In addition, the decreasing emission intensities of indirect excitons with increasing strain are common in 2D layered materials<sup>40,41</sup>.

Moreover, the strain-induced redshift of bandgaps also contributes to the observed redshift in the sub-bandgap CL. Based on the modeled redshift rate of -0.16 eV/%, the strain map in **Figure 3d** can be replotted as the strain-redshift map shown in **Figure 4c**. The increasing strain from the edge to the apex of the tent results in decreasing bandgaps, and the maximum amount of biaxial tensile strain of ~ 2.6% at the apex of the tent corresponds to a CL redshift to ~770 nm, consistent with the maximum observed CL emission wavelength of 780 nm. **Figure 4d** further illustrates the strain-dependent energies of the CBM and VBM, where the position-dependent energy states of the CBM and VBM exhibit funnel shapes consistent with the "Type-I" funneling<sup>1</sup>.

"Type-I" funneling yields bandgap gradients that result in the aggregation of excitons approaching the funnel center<sup>51</sup> and the formation of a "2D exciton reservoir" The exciton drift length is a

critical metric of the effective formation of a 2D exciton reservoir. The effect of the exciton drift length on the number of excitons collected at the funnel center has been extensively studied in 2D materials  $^{1,4,52-54}$ . In order to realize efficient exciton funneling to the center, the exciton drift length  $l_{drift}$  should be set at least the funnel radius R (defined as the distance from the unstrained area to the center),  $l_{drift}$ =R. The exciton drift lengths of GaSe excitons confined by nanoscale strain can be described as  $^{1}$ :

$$l_{drift} = \langle \nu \rangle_{drift} \tau_{1/2} = \frac{\nabla E_{exc}}{m_{exc}} \tau_{dephase} \tau_{1/2}$$

Where  $\tau_{1/2}$  is the exciton lifetime,  $\tau_{dephase}$  is the phase relaxation time, and  $\langle \nu \rangle_{drift}$  is the average drift velocity.  $\nabla E_{exc}$  is the spatial exciton energy gradient and  $m_{exc}$  is the exciton mass. Therefore,  $\nabla E_{exc}$  can be approximated by  $\frac{\Delta E_{exc}}{R}$ , leading to the radius of the funnel R:

$$\mathbf{R} = \sqrt{m_{exc}^{-1} \Delta E_{exc} \tau_{dephase} \tau_{1/2}}$$

In the unstrained region, the energy variation  $\Delta E_{exc}$  of GaSe excitons is ~50 meV<sup>37</sup>. We use the reported translational exciton mass (sum of the effective masses of electron and hole) of GaSe  $2.5m_0$  ( $m_0$  is the electron rest mass:  $0.511 \times 10^6$  eV) obtained from DFT simulation (see more details in Figure S11 of the supporting information), and the dephasing time  $\tau_{dephase}$  of GaSe exciton of ~11 ps<sup>55–57</sup>. The lifetime  $\tau_{1/2}$  of GaSe direct excitons has been reported as ~40-200 ps at 4.2 K<sup>46,58</sup>. Then, the exciton drift length in the unstrained region is calculated as ~1.2–2.8  $\mu m$ , which is larger than the tent radius of ~1.4  $\mu m$ . Thus, excitons can be efficiently funneled to the center of the pillar tent.

Besides, the defect and impurity<sup>59,60</sup> existing in GaSe introduce trap states<sup>46</sup> lying below the band gap. Bound excitons associated with these trapped states overlap in the emission spectrum and exhibit as broad peaks<sup>35,38</sup>. Previous work has demonstrated that pressure<sup>61</sup> and strain gradients<sup>14,15</sup> can cause the shift of these trap states and isolate these discrete energy levels from the continuous energy bands. Intriguingly, these discrete energy states residing in the strain-induced energy funnel show discrete lines, leading to high-intensity counts on the emission spectrum similar to those of quantum wells and quantum dots<sup>62</sup>. Thus, the probability of exciton formation is increased while the non-radiative recombination pathways<sup>63</sup> are decreased, resulting in a higher probability of

emitting photons upon excitation. To summarize, the increasing strain not only creates a "Type-I" funnel by red-shifting the bandgaps but also introduces discrete trap states. The combined effect leads to the observation of enhanced and well-isolated sub-bandgap emission peaks.

## Photon statistics of SPEs under electron-beam and optical excitation

Finally, we performed Hanbury Brown-Twiss (HBT) measurements on the CL and PL from the same pillar region in order to understand the photon correlations associated with the strain localized exciton manifold. Figure 5a illustrates the CL spectrum of an emitter at 627 nm on pillar A. The CL and PL spectral components are not identical to one another as discussed in section 1 of the supplemental information, but based on the NMF decompositions shown in Figures S4c and S6e, we anticipate that the emitter seen here is the same as the emitter seen at 627 nm in Figure S6e. Figure 5b shows the associated photon correlation function with  $g^{(2)}(0) = 2.92 \pm 0.03$  with a time constant of 4.2 ns (fitting details are discussed in Supplementary Section 8). The observed CL bunching is consistent with previous reports of the impulsive high-energy electron excitation of ensembles of emitters<sup>21,25,26</sup>. Figure 5c shows a PL spectrum acquired on pillar A after the CL measurements with an incident power density of 1 nW/ $\mu m^2$ , where this 627 nm emitter is also observed. However, the PL emission shows weak antibunching with  $g^{(2)}(0) = 0.59 \pm 0.06$ , and a time constant of 0.48 ns (Figure 5d) in contrast to the bunching and slower dynamics observed in CL. This 627 nm emission from the PL measurement can be deconvolved into an exciton peak at 1.980 eV (626.2 nm) and two biexciton peaks at 1.979 eV (626.6 nm) and 1.981 eV (625.9 nm) according to the high-resolution PL spectrum shown in Figure S12a. The spectral overlap between the exciton and biexciton features is clearly detrimental to the GaSe exciton SPE purity<sup>16</sup>. Indeed, as shown in Figure S12c, given a larger incident power density of 10 nW/ $\mu m^2$ , the purity of this SPE continues to degrade to  $g^{(2)}(0) = 0.72 \pm 0.07$ , and a shelving state<sup>64,65</sup> related to the interaction between exciton and biexciton states emerges with  $g^{(2)}(\tau) > 1$  for small  $|\tau| > 0$ . The appearance of the shelving state is a result of the increasing impact of radiative biexcitons on the photon statistics with growing incident power density. With this framework in mind, the CL bunching observed here can be explained as a result of a radiative biexciton cascade<sup>66–69</sup>.

Moreover, we characterized another SPE on pillar A at 694 nm (as shown in **Figures 5e and 5f**) by PL excitation and observed  $g^{(2)}(0) = 0.43 \pm 0.04$  and a decay time-constant of  $\sim 0.2\pm0.02$  ns

(using a 128 ps time bin). We anticipate that the 694 nm PL observed here originates from the same emitter seen in the 703 nm CL component shown in Figure S5e and the 694 nm PL component shown in Figure S6h. This emitter can also be deconvolved into an exciton peak at 1.792 eV (692 nm) and a biexciton peak at 1.787 eV (694 nm), as described and identified by power-dependent measurements shown in supplementary **Figure S13**. Also, the power-dependent PL antibunching of this SPE is summarized in **Figures S14a** and **S14b**. Notably, neither emitter exhibited any changes in photophysics induced by the electron-beam.

#### **Conclusion**

In conclusion, correlative cathodoluminescence, photoluminescence, and atomic force microscopies complemented by DFT modeling provide a true nanoscale picture of strain-localized SPEs in GaSe. The strain-localized SPEs are with a broad range of emission wavelengths from 620 nm to 900 nm. We show substantial strain-controlled tuning of localized excitons across a ~ 100 nm bandwidth. A "Type-I" energy funneling effect leads to luminescence enhancement and redshift with increasing strain. With higher exciton densities at the funnel center, radiative recombination from exciton complexes (excitons and biexcitons) that are associated with trap states are significantly enhanced compared to those in the unstrained area. CL photon bunching with a 4.2 ns time constant was observed and attributed to radiative biexciton cascade processes. Despite the challenge of probing CL antibunching in excitonic complexes, our PL measurements on the same pillar confirm the presence of isolated SPEs. The observation of PL antibunching after CL measurements also highlight the stability of these GaSe SPEs. The combined nanoscale understanding of strain-induced SPE dynamics and energetics provided by these correlative microscopies provides a framework for the deterministic generation of bright and robust GaSe SPEs with highly controllable and tunable wavelengths. More broadly, a nanoscale understanding of strain and exciton funneling should translate to many other classes of SPEs in 2D materials and provide critical insights for other photonic applications such as lasing, photovoltaic conversion, and optical detection.

**Methods.** Preparation of GaSe samples. Bulk GaSe was synthesized using the chemical vapor transport (CVT) method<sup>70</sup> as described in our previous work<sup>16</sup>. The GaSe flakes with various thicknesses are obtained through mechanical exfoliation of the high-quality bulk crystals.

Fabrication of SiO<sub>2</sub> nanopillars and dry transfer of GaSe flakes: Nanopillar (150 nm, 200 nm, and 250 nm in diameter) arrays were fabricated via electron beam lithography. The GaSe flakes with various thicknesses are obtained through mechanical exfoliation of the high-quality bulk crystals and then transferred to the nanopillars. The details could be referred to in our previous work<sup>16</sup>.

*Photoluminescence spectroscopy.* The cryo-PL and associated photon statistics measurements were performed in a home-built confocal PL microscope in a backscattering configuration. A Princeton Instruments Isoplane SCT-320 spectrograph with a PIXIS 400BR Excelon camera and a grating turret with 150 g/mm, 600 g/mm, and 2400 g/mm gratings were used to measure PL spectra with spectral resolutions of  $\sim 3.25$  meV,  $\sim 300~\mu$ eV, and  $\sim 30~\mu$ eV, respectively. A 532 nm diode laser (Cobolt) was used for excitation. A 100x in-vacuum objective (Zeiss, NA = 0.85) was integrated with the Montana S100 closed-cycle cryostat. The PL mapping was controlled by 2-axis galvo scanning. The photon-antibunching measurements utilized a pair of large-area superconducting nanowire single-photon detectors (SNSPDs, Quantum Opus) and a Swabian Time Tagger 20 time-correlated single photon counting (TCSPC) system. A 90:10 non-polarizing beam splitter was used to allow for PL (10% coupling efficiency) and photon correlation functions (90% coupling efficiency) to be acquired in parallel.

Cathodoluminescence microscopy. The cathodoluminescence microscopies were performed in an FEI Quattro SEM with a Gatan dual fuel cryostage and a Delmic Sparc cathodoluminescence module. The sample was cooled to 9 K with liquid helium, and all spectra were acquired on an Andor Kymera spectrograph with an Andor Newton CCD camera. All CL photon statistics measurements were performed by fiber coupling the CL into the same SNSPDs used for the photoluminescence measurements.

Monte Carlo simulations of electron interaction volume in GaSe: Monte Carlo simulations were performed to calculate the electron interaction volume in GaSe by the CASINO program<sup>13,14</sup>. More details can be referred to Section S11, Figures S15 and S16 of supporting information.

DFT simulations. Plane-wave DFT calculations were carried out using the Vienna Ab initio Simulation Package<sup>28,29</sup> (VASP) with projector augmented wave (PAW) pseudopotentials<sup>28,30,31</sup> for electron-ion interactions, and the generalized gradient approximation (GGA) functional of Perdew, Burke and Ernzerhof<sup>71</sup> (PBE) for exchange-correlation interactions. The details of geometry optimization of bulk GaSe was shown in our previous work<sup>16</sup>. The electronic band structure post-analysis was carried out using the VASPKIT package<sup>72</sup>.

#### ASSOCIATED CONTENT

The authors declare no competing financial interest. An initial draft of this work was uploaded to the arXiv preprint server on May 5, 2023, as the following reference: Weijun Luo, Benjamin Lawrie, Alexander Puretzky, Qishuo Tan, Gage Eichman, Edward Mcgee, Anna Swan, Liangbo Liang, and Xi Ling. "Imaging Strain-Localized Single-Photon Emitters in Layered GaSe below the Diffraction Limit." arXiv:2310.00910. https://arxiv.org/abs/2310.00910 (accessed May 5, 2023).

#### SUPPORTING INFORMATION

The Supporting Information is available free of charge at XXX. Description of statistics of maximum emission wavelengths, NMF decomposition of CL mapping results, Power-dependent PL spectra, and Power-dependent photon-antibunching results (PDF).

#### **ACKNOWLEDGEMENTS**

This material is based upon work supported by the National Science Foundation (NSF) under Grant No. (1945364). Work by X.L. was supported by the U.S. Department of Energy (DOE), Office of Science, Basic Energy Sciences (BES) under Award DE-SC0021064. W.L., X.L. and A.K.S acknowledge the support of National Science Foundation (NSF) under Grant No. (2111160). The CL microscopy was supported by the U.S. Department of Energy, Office of Science, National Quantum Information Science Research Centers, Quantum Science Center. The PL and CL spectroscopies were supported by the Center for Nanophase Materials Sciences (CNMS), which is a US Department of Energy Office of Science User Facility. X.L. and A.K.S. acknowledge the membership of the Photonics Center at Boston University. The computational

work is performed using Shared Computing Cluster (BUSCC) at Boston University.

#### **AUTHOR CONTRIBUTIONS**

W.L., B.L., A.P., and X.L. conceived the experiment. Q.T. synthesized and characterized the bulk GaSe crystals. W.L. prepared samples with assistance from Q.T., and H.G. B.L. performed the CL microscopy and CL photon statistics measurements. W.L. conducted the PL / photon-statistics measurements with assistance from A.P. and B.L. W.L performed theoretical calculations with assistance from L.L. W.L performed the analysis and interpretation of the data with assistance from A.P., B.L., G.E., E.M., D.B.L., L.L., A.K.S., and X.L. All authors contributed to the writing of the manuscript.

#### **AUTHOR INFORMATION**

#### **Lead Contact**

Further information and requests for resources and materials should be directed and will be fulfilled by the Lead Contact, Xi Ling (xiling@bu.edu).

The authors declare no competing financial interest.

#### **Materials Availability**

All materials generated in this study are available upon reasonable request to the lead contact.

#### **Data and Code Availability**

All data needed to evaluate the conclusions of the paper are present in the paper and/or Supplemental Information. Additional data related to this paper may be requested from the authors.

#### REFERENCES

- (1) Feng, J.; Qian, X.; Huang, C.-W.; Li, J. Strain-Engineered Artificial Atom as a Broad-Spectrum Solar Energy Funnel. *Nat. Photonics* **2012**, *6* (12), 866.
- (2) San-Jose, P.; Parente, V.; Guinea, F.; Roldán, R.; Prada, E. Inverse Funnel Effect of Excitons in Strained Black Phosphorus. *Phys. Rev. X* **2016**, *6* (3), 031046.
- (3) Castellanos-Gomez, A.; Roldán, R.; Cappelluti, E.; Buscema, M.; Guinea, F.; van der Zant, H. S.; Steele, G. A. Local Strain Engineering in Atomically Thin MoS2. *Nano Lett.* **2013**, *13* (11), 5361–5366.
- (4) Li, H.; Contryman, A. W.; Qian, X.; Ardakani, S. M.; Gong, Y.; Wang, X.; Weisse, J. M.; Lee, C. H.; Zhao, J.; Ajayan, P. M. Optoelectronic Crystal of Artificial Atoms in Strain-Textured Molybdenum Disulphide. *Nat. Commun.* **2015**, *6* (1), 1–7.
- (5) Lloyd, D.; Liu, X.; Christopher, J. W.; Cantley, L.; Wadehra, A.; Kim, B. L.; Goldberg, B. B.; Swan, A. K.; Bunch, J. S. Band Gap Engineering with Ultralarge Biaxial Strains in Suspended Monolayer MoS2. *Nano Lett.* **2016**, *16* (9), 5836–5841.
- (6) Moon, H.; Grosso, G.; Chakraborty, C.; Peng, C.; Taniguchi, T.; Watanabe, K.; Englund, D. Dynamic Exciton Funneling by Local Strain Control in a Monolayer Semiconductor. *Nano Lett.* **2020**, *20* (9), 6791–6797.
- (7) Tran, T. T.; Bray, K.; Ford, M. J.; Toth, M.; Aharonovich, I. Quantum Emission from Hexagonal Boron Nitride Monolayers. *Nat. Nanotechnol.* **2016**, *11* (1), 37.
- (8) Tran, T. T.; Elbadawi, C.; Totonjian, D.; Lobo, C. J.; Grosso, G.; Moon, H.; Englund, D. R.; Ford, M. J.; Aharonovich, I.; Toth, M. Robust Multicolor Single Photon Emission from Point Defects in Hexagonal Boron Nitride. *ACS Nano* **2016**, *10* (8), 7331–7338.
- (9) Grosso, G.; Moon, H.; Lienhard, B.; Ali, S.; Efetov, D. K.; Furchi, M. M.; Jarillo-Herrero, P.; Ford, M. J.; Aharonovich, I.; Englund, D. Tunable and High-Purity Room Temperature Single-Photon Emission from Atomic Defects in Hexagonal Boron Nitride. *Nat. Commun.* **2017**, 8 (1), 705.
- (10) He, Y.-M.; Clark, G.; Schaibley, J. R.; He, Y.; Chen, M.-C.; Wei, Y.-J.; Ding, X.; Zhang, Q.; Yao, W.; Xu, X.; Lu, C.-Y.; Pan, J.-W. Single Quantum Emitters in Monolayer Semiconductors. *Nat. Nanotechnol.* **2015**, *10* (6), 497–502. https://doi.org/10.1038/nnano.2015.75.
- (11) Koperski, M.; Nogajewski, K.; Arora, A.; Cherkez, V.; Mallet, P.; Veuillen, J.-Y.; Marcus, J.; Kossacki, P.; Potemski, M. Single Photon Emitters in Exfoliated WSe 2 Structures. *Nat. Nanotechnol.* **2015**, *10* (6), 503.
- (12) Srivastava, A.; Sidler, M.; Allain, A. V.; Lembke, D. S.; Kis, A.; Imamoğlu, A. Optically Active Quantum Dots in Monolayer WSe2. *Nat. Nanotechnol.* **2015**, *10* (6), 491–496. https://doi.org/10.1038/nnano.2015.60.
- (13) Palacios-Berraquero, C.; Kara, D. M.; Montblanch, A. R.-P.; Barbone, M.; Latawiec, P.; Yoon, D.; Ott, A. K.; Loncar, M.; Ferrari, A. C.; Atatüre, M. Large-Scale Quantum-Emitter Arrays in Atomically Thin Semiconductors. *Nat. Commun.* **2017**, *8* (1), 15093. https://doi.org/10.1038/ncomms15093.
- (14) Branny, A.; Kumar, S.; Proux, R.; Gerardot, B. D. Deterministic Strain-Induced Arrays of Quantum Emitters in a Two-Dimensional Semiconductor. *Nat. Commun.* **2017**, *8* (1), 15053. https://doi.org/10.1038/ncomms15053.
- (15) Parto, K.; Azzam, S. I.; Banerjee, K.; Moody, G. Defect and Strain Engineering of Monolayer WSe2 Enables Site-Controlled Single-Photon Emission up to 150 K. *Nat. Commun.* **2021**, *12* (1), 1–8.

- (16) Luo, W.; Puretzky, A. A.; Lawrie, B. J.; Tan, Q.; Gao, H.; Chen, Z.; Sergienko, A. V.; Swan, A. K.; Liang, L.; Ling, X. Deterministic Localization of Strain-Induced Single-Photon Emitters in Multilayer GaSe. *ACS Photonics* **2023**, *10* (8), 2530–2539. https://doi.org/10.1021/acsphotonics.3c00052.
- (17) Kulig, M.; Zipfel, J.; Nagler, P.; Blanter, S.; Schüller, C.; Korn, T.; Paradiso, N.; Glazov, M. M.; Chernikov, A. Exciton Diffusion and Halo Effects in Monolayer Semiconductors. *Phys. Rev. Lett.* **2018**, *120* (20), 207401.
- (18) Cadiz, F.; Robert, C.; Courtade, E.; Manca, M.; Martinelli, L.; Taniguchi, T.; Watanabe, K.; Amand, T.; Rowe, A. C. H.; Paget, D. Exciton Diffusion in WSe2 Monolayers Embedded in a van Der Waals Heterostructure. *Appl. Phys. Lett.* **2018**, *112* (15), 152106.
- (19) Uddin, S. Z.; Kim, H.; Lorenzon, M.; Yeh, M.; Lien, D.-H.; Barnard, E. S.; Htoon, H.; Weber-Bargioni, A.; Javey, A. Neutral Exciton Diffusion in Monolayer MoS2. *ACS Nano* **2020**, *14* (10), 13433–13440.
- (20) Kern, J.; Niehues, I.; Tonndorf, P.; Schmidt, R.; Wigger, D.; Schneider, R.; Stiehm, T.; Michaelis de Vasconcellos, S.; Reiter, D. E.; Kuhn, T.; Bratschitsch, R. Nanoscale Positioning of Single-Photon Emitters in Atomically Thin WSe 2. *Adv. Mater.* **2016**, *28* (33), 7101–7105. https://doi.org/10.1002/adma.201600560.
- (21) Meuret, S.; Tizei, L. H. G.; Cazimajou, T.; Bourrellier, R.; Chang, H. C.; Treussart, F.; Kociak, M. Photon Bunching in Cathodoluminescence. *Phys. Rev. Lett.* **2015**, *114* (19), 197401.
- (22) Bourrellier, R.; Meuret, S.; Tararan, A.; Stéphan, O.; Kociak, M.; Tizei, L. H.; Zobelli, A. Bright UV Single Photon Emission at Point Defects in H-BN. *Nano Lett.* **2016**, *16* (7), 4317–4321.
- (23) Hayee, F.; Yu, L.; Zhang, J. L.; Ciccarino, C. J.; Nguyen, M.; Marshall, A. F.; Aharonovich, I.; Vučković, J.; Narang, P.; Heinz, T. F.; Dionne, J. A. Revealing Multiple Classes of Stable Quantum Emitters in Hexagonal Boron Nitride with Correlated Cathodoluminescence, Photoluminescence, and Strain Mapping. *Nat. Mater.* **2020**, *19* (5), 534–539. https://doi.org/10.1038/s41563-020-0616-9.
- (24) Curie, D.; Krogel, J. T.; Cavar, L.; Solanki, A.; Upadhyaya, P.; Li, T.; Pai, Y.-Y.; Chilcote, M.; Iyer, V.; Puretzky, A.; Ivanov, I.; Du, M.-H.; Reboredo, F.; Lawrie, B. Correlative Nanoscale Imaging of Strained hBN Spin Defects. *ACS Appl. Mater. Interfaces* **2022**, *14* (36), 41361–41368. https://doi.org/10.1021/acsami.2c11886.
- (25) Feldman, M. A.; Dumitrescu, E. F.; Bridges, D.; Chisholm, M. F.; Davidson, R. B.; Evans, P. G.; Hachtel, J. A.; Hu, A.; Pooser, R. C.; Haglund, R. F.; Lawrie, B. J. Colossal Photon Bunching in Quasiparticle-Mediated Nanodiamond Cathodoluminescence. *Phys. Rev. B* **2018**, *97* (8), 081404. https://doi.org/10.1103/PhysRevB.97.081404.
- (26) Iyer, V.; Roccapriore, K.; Ng, J.; Srijanto, B.; Lingerfelt, D.; Lawrie, B. Photon Bunching in Cathodoluminescence Induced by Indirect Electron Excitation. arXiv January 25, 2023. https://doi.org/10.48550/arXiv.2301.10708.
- (27) Park, K.-D.; May, M. A.; Leng, H.; Wang, J.; Kropp, J. A.; Gougousi, T.; Pelton, M.; Raschke, M. B. Tip-Enhanced Strong Coupling Spectroscopy, Imaging, and Control of a Single Quantum Emitter. *Sci. Adv.* **2019**, *5* (7), eaav5931.
- (28) Lange, L.; Schäfer, F.; Biewald, A.; Ciesielski, R.; Hartschuh, A. Controlling Photon Antibunching from 1D Emitters Using Optical Antennas. *Nanoscale* **2019**, *11* (31), 14907–14911.

- (29) Darlington, T. P.; Carmesin, C.; Florian, M.; Yanev, E.; Ajayi, O.; Ardelean, J.; Rhodes, D. A.; Ghiotto, A.; Krayev, A.; Watanabe, K.; Taniguchi, T.; Kysar, J. W.; Pasupathy, A. N.; Hone, J. C.; Jahnke, F.; Borys, N. J.; Schuck, P. J. Imaging Strain-Localized Exciton States in Nanoscale Bubbles in Monolayer WSe2 at Room Temperature. *ArXiv200301789 Cond-Mat* **2020**.
- (30) Martín-Jiménez, A.; Jover, Ó.; Lauwaet, K.; Granados, D.; Miranda, R.; Otero, R. Selectively Addressing Plasmonic Modes and Excitonic States in a Nanocavity Hosting a Quantum Emitter. *Nano Lett.* **2022**, *22* (23), 9283–9289. https://doi.org/10.1021/acs.nanolett.2c02758.
- (31) Zheng, S.; So, J.-K.; Liu, F.; Liu, Z.; Zheludev, N.; Fan, H. J. Giant Enhancement of Cathodoluminescence of Monolayer Transitional Metal Dichalcogenides Semiconductors. *Nano Lett.* **2017**, *17* (10), 6475–6480.
- (32) Yang, W.-C.; Chuang, H.-J.; Rosenberger, M.; McCreary, K.; Jonker, B.; Sharma, R. Probing Electronic Structures of Monolayer WSe2 Stacked with hBN Using Correlative Cathodoluminescence and Electron Energy-Loss Spectroscopy. *Microsc. Microanal.* **2021**, 27 (S1), 1174–1176.
- (33) Zheng, L.; Liu, Z.; Liu, D.; Wang, X.; Li, Y.; Jiang, M.; Lin, F.; Zhang, H.; Shen, B.; Zhu, X. Deep Subwavelength Control of Valley Polarized Cathodoluminescence in H-BN/WSe2/h-BN Heterostructure. *Nat. Commun.* **2021**, *12* (1), 291.
- (34) Roux, S.; Fournier, C.; Watanabe, K.; Taniguchi, T.; Hermier, J.-P.; Barjon, J.; Delteil, A. Cathodoluminescence Monitoring of Quantum Emitter Activation in Hexagonal Boron Nitride. *Appl. Phys. Lett.* **2022**, *121* (18), 184002.
- (35) Tonndorf, P.; Schwarz, S.; Kern, J.; Niehues, I.; Del Pozo-Zamudio, O.; Dmitriev, A. I.; Bakhtinov, A. P.; Borisenko, D. N.; Kolesnikov, N. N.; Tartakovskii, A. I. Single-Photon Emitters in GaSe. 2D Mater. 2017, 4 (2), 021010.
- (36) Tonndorf, P.; Del Pozo-Zamudio, O.; Gruhler, N.; Kern, J.; Schmidt, R.; Dmitriev, A. I.; Bakhtinov, A. P.; Tartakovskii, A. I.; Pernice, W.; Michaelis de Vasconcellos, S. On-Chip Waveguide Coupling of a Layered Semiconductor Single-Photon Source. *Nano Lett.* **2017**, *17* (9), 5446–5451.
- (37) Capozzi, V. Direct and Indirect Excitonic Emission in GaSe. Phys. Rev. B 1981, 23 (2), 836.
- (38) Wei, C.; Chen, X.; Li, D.; Su, H.; He, H.; Dai, J.-F. Bound Exciton and Free Exciton States in GaSe Thin Slab. *Sci. Rep.* **2016**, *6* (1), 1–6.
- (39) Luo, W. Arenasluo/Gase\_cl\_2023, 2023. https://github.com/arenasluo/gase\_cl\_2023 (accessed 2023-06-01).
- (40) Yu, Y.; Dong, C.-D.; Binder, R.; Schumacher, S.; Ning, C.-Z. Strain-Induced Indirect-to-Direct Bandgap Transition, Photoluminescence Enhancement, and Linewidth Reduction in Bilayer MoTe2. *ACS Nano* **2023**, *17* (5), 4230–4238.
- (41) Conley, H. J.; Wang, B.; Ziegler, J. I.; Haglund Jr, R. F.; Pantelides, S. T.; Bolotin, K. I. Bandgap Engineering of Strained Monolayer and Bilayer MoS2. *Nano Lett.* **2013**, *13* (8), 3626–3630.
- (42) Matsumura, T.; Sudo, M.; Tatsuyama, C.; Ichimura, S. Photoluminescence in GaSe. *Phys. Status Solidi A* **1977**, *43* (2), 685–693.
- (43) Capozzi, V.; Montagna, M. Optical Spectroscopy of Extrinsic Recombinations in Gallium Selenide. *Phys. Rev. B* **1989**, *40* (5), 3182.
- (44) Ziegler, J.; Klaiss, R.; Blaikie, A.; Miller, D.; Horowitz, V. R.; Alemán, B. J. Deterministic Quantum Emitter Formation in Hexagonal Boron Nitride via Controlled Edge Creation. *Nano Lett.* **2019**, *19* (3), 2121–2127. https://doi.org/10.1021/acs.nanolett.9b00357.

- (45) Li, C.; Mendelson, N.; Ritika, R.; Chen, Y.; Xu, Z.-Q.; Toth, M.; Aharonovich, I. Scalable and Deterministic Fabrication of Quantum Emitter Arrays from Hexagonal Boron Nitride. *Nano Lett.* **2021**, *21* (8), 3626–3632.
- (46) Del Pozo-Zamudio, O.; Schwarz, S.; Sich, M.; Akimov, I. A.; Bayer, M.; Schofield, R. C.; Chekhovich, E. A.; Robinson, B. J.; Kay, N. D.; Kolosov, O. V. Photoluminescence of Two-Dimensional GaTe and GaSe Films. *2D Mater.* **2015**, *2* (3), 035010.
- (47) Luo, Y.; Shepard, G. D.; Ardelean, J. V.; Rhodes, D. A.; Kim, B.; Barmak, K.; Hone, J. C.; Strauf, S. Deterministic Coupling of Site-Controlled Quantum Emitters in Monolayer WSe 2 to Plasmonic Nanocavities. *Nat. Nanotechnol.* **2018**, *13* (12), 1137.
- (48) Montcuquet, A.-S.; Hervé, L.; Garcia, F. P. N. Y.; Dinten, J.-M.; Mars, J. I. Nonnegative Matrix Factorization: A Blind Spectra Separation Method for in Vivo Fluorescent Optical Imaging. *J. Biomed. Opt.* **2010**, *15* (5), 056009.
- (49) Gobinet, C.; Perrin, E.; Huez, R. Application of Non-Negative Matrix Factorization to Fluorescence Spectroscopy. In 2004 12th European Signal Processing Conference; IEEE, 2004; pp 1095–1098.
- (50) Iyer, V.; Phang, Y. S.; Butler, A.; Chen, J.; Lerner, B.; Argyropoulos, C.; Hoang, T.; Lawrie, B. Near-Field Imaging of Plasmonic Nanopatch Antennas with Integrated Semiconductor Quantum Dots. *APL Photonics* **2021**, *6* (10), 106103. https://doi.org/10.1063/5.0065524.
- (51) Fu, X.; Su, C.; Fu, Q.; Zhu, X.; Zhu, R.; Liu, C.; Liao, Z.; Xu, J.; Guo, W.; Feng, J. Tailoring Exciton Dynamics by Elastic Strain-Gradient in Semiconductors. *Adv. Mater.* **2014**, *26* (16), 2572–2579.
- (52) Dirnberger, F.; Ziegler, J. D.; Faria Junior, P. E.; Bushati, R.; Taniguchi, T.; Watanabe, K.; Fabian, J.; Bougeard, D.; Chernikov, A.; Menon, V. M. Quasi-1D Exciton Channels in Strain-Engineered 2D Materials. *Sci. Adv.* **2021**, *7* (44), eabj3066.
- (53) Datta, K.; Lyu, Z.; Li, Z.; Taniguchi, T.; Watanabe, K.; Deotare, P. B. Spatiotemporally Controlled Room-Temperature Exciton Transport under Dynamic Strain. *Nat. Photonics* **2022**, *16* (3), 242–247.
- (54) Lee, H.; Koo, Y.; Choi, J.; Kumar, S.; Lee, H.-T.; Ji, G.; Choi, S. H.; Kang, M.; Kim, K. K.; Park, H.-R. Drift-Dominant Exciton Funneling and Trion Conversion in 2D Semiconductors on the Nanogap. *Sci. Adv.* **2022**, *8* (5), eabm5236.
- (55) Yamamoto, M.; Mino, H.; Akai, I.; Karasawa, T.; Aguekian, V. F. Space-Resolved Luminescence and Degenerate Four-Wave-Mixing Spectra of Heavily Photo-Created Exciton States in a Layered Crystal GaSe. *J. Lumin.* **2000**, *87*, 275–277.
- (56) Zalamai, V. V.; Syrbu, N. N.; Stamov, I. G.; Beril, S. I. Wannier-Mott Excitons in GaSe Single Crystals. *J. Opt.* **2020**, *22* (8), 085402.
- (57) Zalamai, V. V.; Stamov, I. G.; Syrbu, N. N. Interference of Exciton-Polariton Waves in GaSe Nanocrystals. *Mater. Today Commun.* **2021**, *27*, 102355.
- (58) Kushida, T.; Minami, F.; Oka, Y.; Nakazaki, Y.; Tanaka, Y. Population Dynamics and Spin Relaxations of Excitons in GaSe. *Il Nuovo Cimento B 1971-1996* **1977**, *39* (2), 650–654.
- (59) Hopkinson, D. G.; Zólyomi, V.; Rooney, A. P.; Clark, N.; Terry, D. J.; Hamer, M.; Lewis, D. J.; Allen, C. S.; Kirkland, A. I.; Andreev, Y. Formation and Healing of Defects in Atomically Thin GaSe and InSe. *ACS Nano* **2019**, *13* (5), 5112–5123.
- (60) Kokh, K. A.; Atuchin, V. V.; Gavrilova, T. A.; Kozhukhov, A.; Maximovskiy, E. A.; Pokrovsky, L. D.; Tsygankova, A. R.; Saprykin, A. I. Defects in GaSe Grown by Bridgman Method. *J. Microsc.* **2014**, *256* (3), 208–212.

- (61) Ye, Y.; Dou, X.; Ding, K.; Chen, Y.; Jiang, D.; Yang, F.; Sun, B. Single Photon Emission from Deep-Level Defects in Monolayer WS e 2. *Phys. Rev. B* **2017**, *95* (24), 245313. https://doi.org/10.1103/PhysRevB.95.245313.
- (62) Davies, J. H. *The Physics of Low-Dimensional Semiconductors: An Introduction*; Cambridge university press, 1998.
- (63) David, A.; Miller, B. Optical Physics of Quantum Wells. In *Quantum Dynamics of Simple Systems*; CRC Press, 2020; pp 239–266.
- (64) Pomeau, Y.; Tran, M.-B.; Pomeau, Y.; Tran, M.-B. The Statistical Theory of Shelving. *Stat. Phys. Non Equilib. Quantum Phenom.* **2019**, 35–39.
- (65) Berthel, M.; Mollet, O.; Dantelle, G.; Gacoin, T.; Huant, S.; Drezet, A. Photophysics of Single Nitrogen-Vacancy Centers in Diamond Nanocrystals. *Phys. Rev. B* **2015**, *91* (3), 035308.
- (66) Heindel, T.; Thoma, A.; von Helversen, M.; Schmidt, M.; Schlehahn, A.; Gschrey, M.; Schnauber, P.; Schulze, J.-H.; Strittmatter, A.; Beyer, J. A Bright Triggered Twin-Photon Source in the Solid State. *Nat. Commun.* **2017**, *8* (1), 14870.
- (67) Braun, T.; Unsleber, S.; Baumann, V.; Gschrey, M.; Rodt, S.; Reitzenstein, S.; Schneider, C.; Höfling, S.; Kamp, M. Cascaded Emission of Linearly Polarized Single Photons from Positioned InP/GaInP Quantum Dots. *Appl. Phys. Lett.* **2013**, *103* (19), 191113.
- (68) Rodt, S.; Reitzenstein, S.; Heindel, T. Deterministically Fabricated Solid-State Quantum-Light Sources. *J. Phys. Condens. Matter* **2020**, *32* (15), 153003.
- (69) Schmidt, G.; Berger, C.; Dadgar, A.; Bertram, F.; Veit, P.; Metzner, S.; Strittmatter, A.; Christen, J.; Jagsch, S. T.; Wagner, M. R. Nitride Microcavities and Single Quantum Dots for Classical and Non-Classical Light Emitters. *Semicond. Nanophotonics Mater. Models Devices* **2020**, 453–504.
- (70) Ishii, T.; Kambe, N. GaSe Single Crystal Growth by Iodine Vapor Transport. *J. Cryst. Growth* **1986**, 76 (2), 489–493.
- (71) Perdew, J. P.; Burke, K.; Ernzerhof, M. Generalized Gradient Approximation Made Simple. *Phys. Rev. Lett.* **1996**, *77* (18), 3865.
- (72) Wang, V.; Xu, N.; Liu, J.-C.; Tang, G.; Geng, W.-T. VASPKIT: A User-Friendly Interface Facilitating High-Throughput Computing and Analysis Using VASP Code. *Comput. Phys. Commun.* **2021**, *267*, 108033.

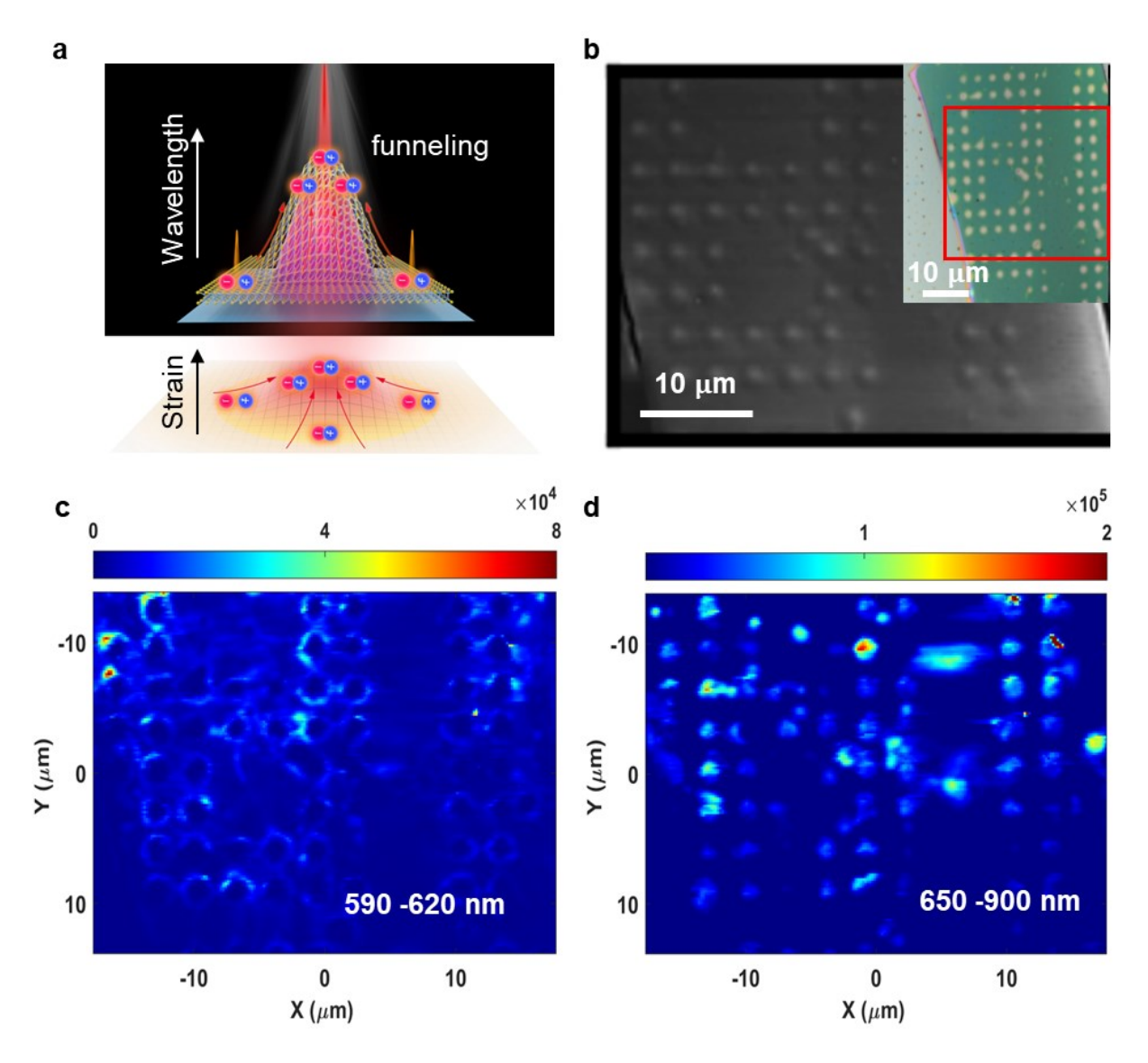


Figure 1. CL imaging of GaSe flakes on SiO<sub>2</sub> nanopillar arrays. (a) Illustration of GaSe on the nanopillar and exciton funneling effect. (b) SEM and inset optical images of a 150-nm-thick GaSe flake tented on a SiO<sub>2</sub> nanopillar array. (c) CL intensity map integrated across wavelengths of 590-620 nm for a representative array of pillars (highlighted area in (b)) measured at T = 9 K, with an incident electron beam energy of 5 keV, a beam current of 28 pA, and a spatial resolution of 180 nm. (d) CL intensity map integrated across wavelengths of 650-900 nm for the same representative array of pillars measured at T = 9 K.

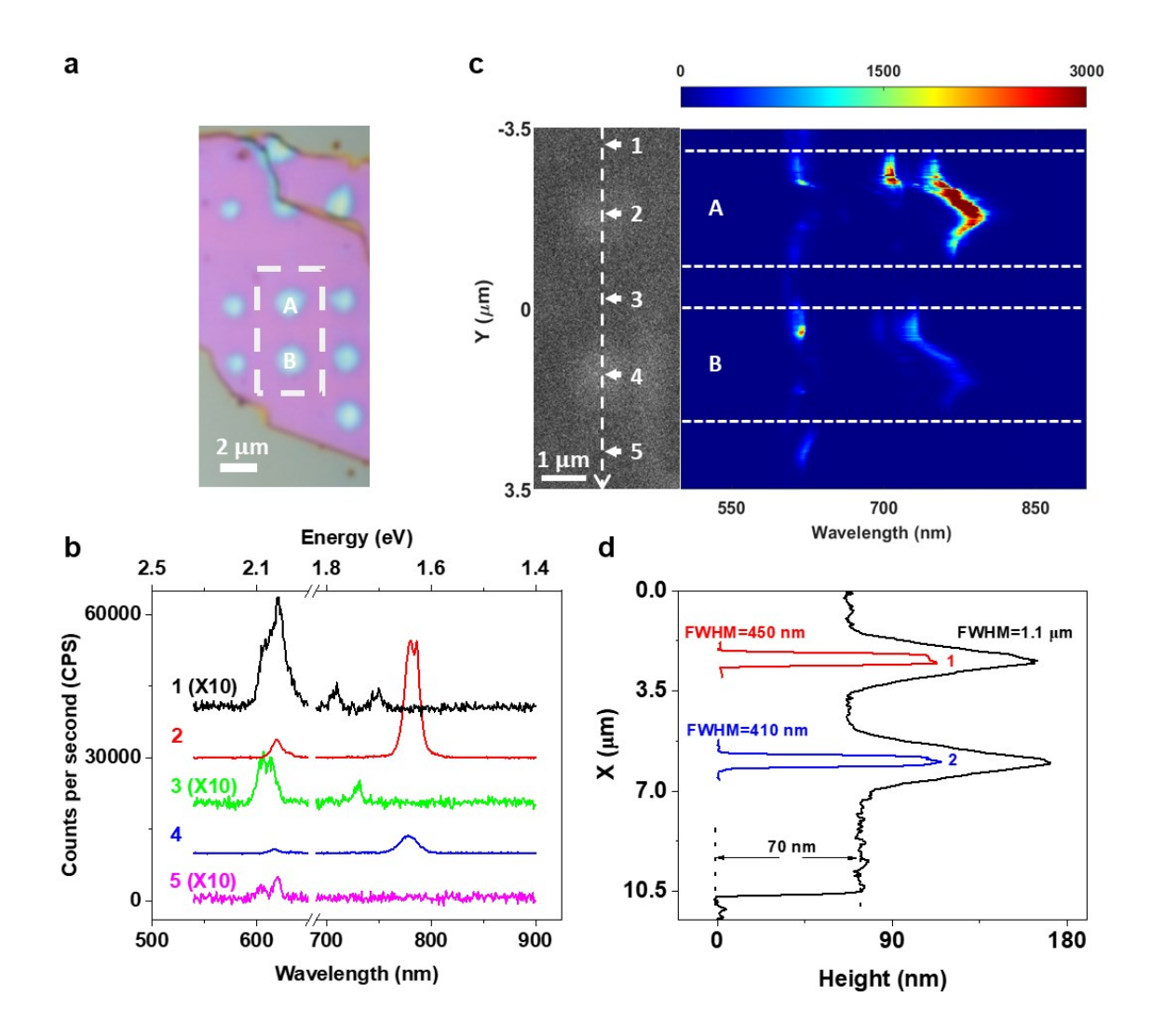


Figure 2. CL line scan of GaSe flakes on SiO<sub>2</sub> nanopillar arrays. (a) Optical image of a 70-nm-thick GaSe flake tented on a SiO<sub>2</sub> nanopillar array. CL line scan measurements are performed along Pillars A and B. The scale bar is 2  $\mu$ m. (b) Five representative CL spectra from positions 1 – 5, as labeled in the left panel of (c). The intensities of spectra 1, 3, and 5 are scaled up 10-fold for comparison with the other spectra. (c) left panel: SEM image of the highlighted area in (a). The scale bar is 1  $\mu$ m. The vertical dashed white arrow shows the CL line scan path. The right panel shows the CL line scan acquired with 20 nm spatial resolution measured at T = 9 K. The horizontal dashed lines are guides to the positions 1 – 5 where the CL spectra were collected. (d) AFM height profiles of tents A and B (black), and the associated SiO<sub>2</sub> pillars A (red) and B (blue).

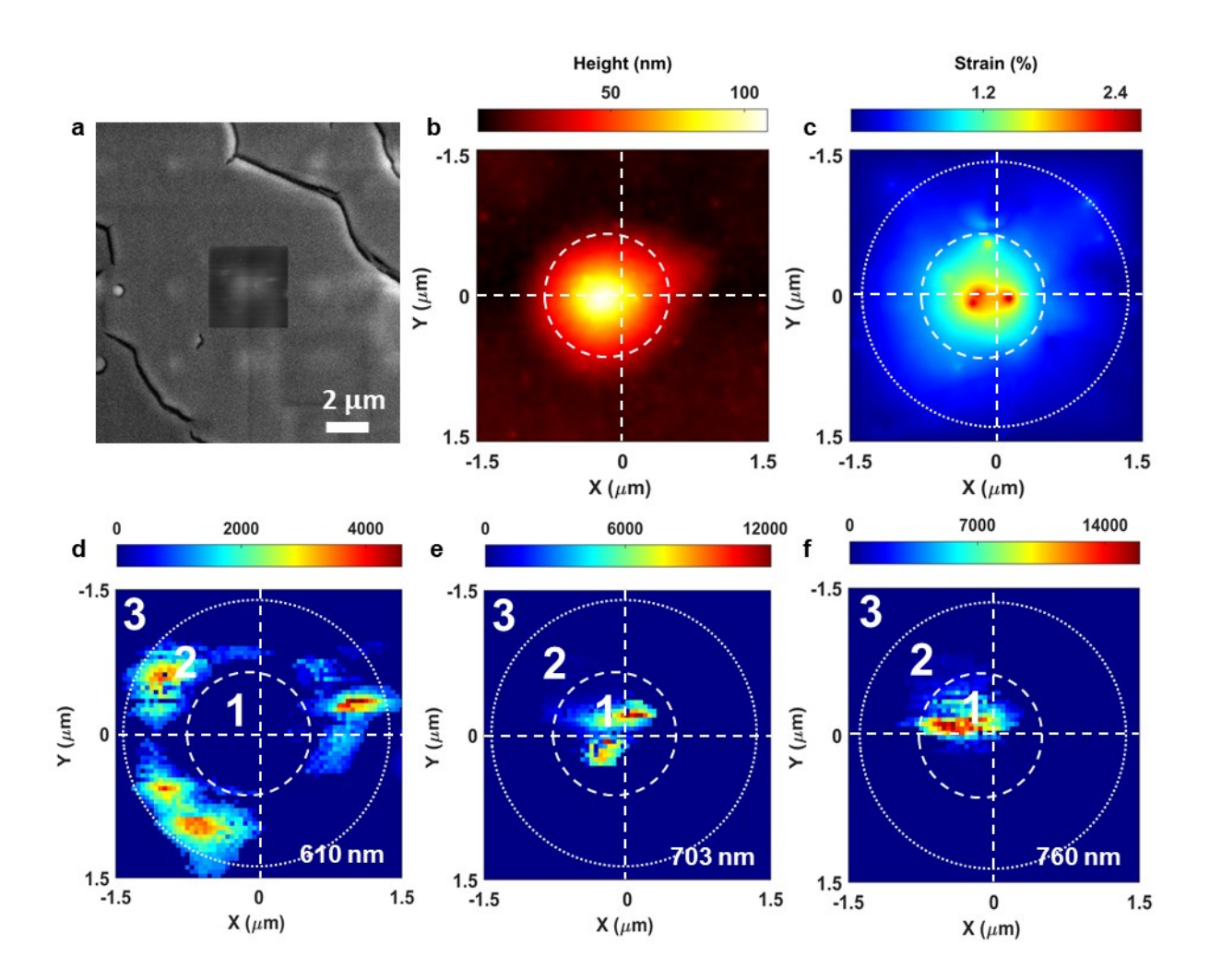


Figure 3. NMF decomposition of CL spectrum image measured at T=9 K. (a) SEM image of pillar A (labeled in Figure 2a) for CL mapping. (b) AFM image of pillar A, dashed lines are guides to the eye. (c) Simulated strain distribution over the pillar according to AFM height profile in (b). (d) – (f) Intensity maps of three emissions at 610 nm, 703 nm, and 760 nm, respectively.

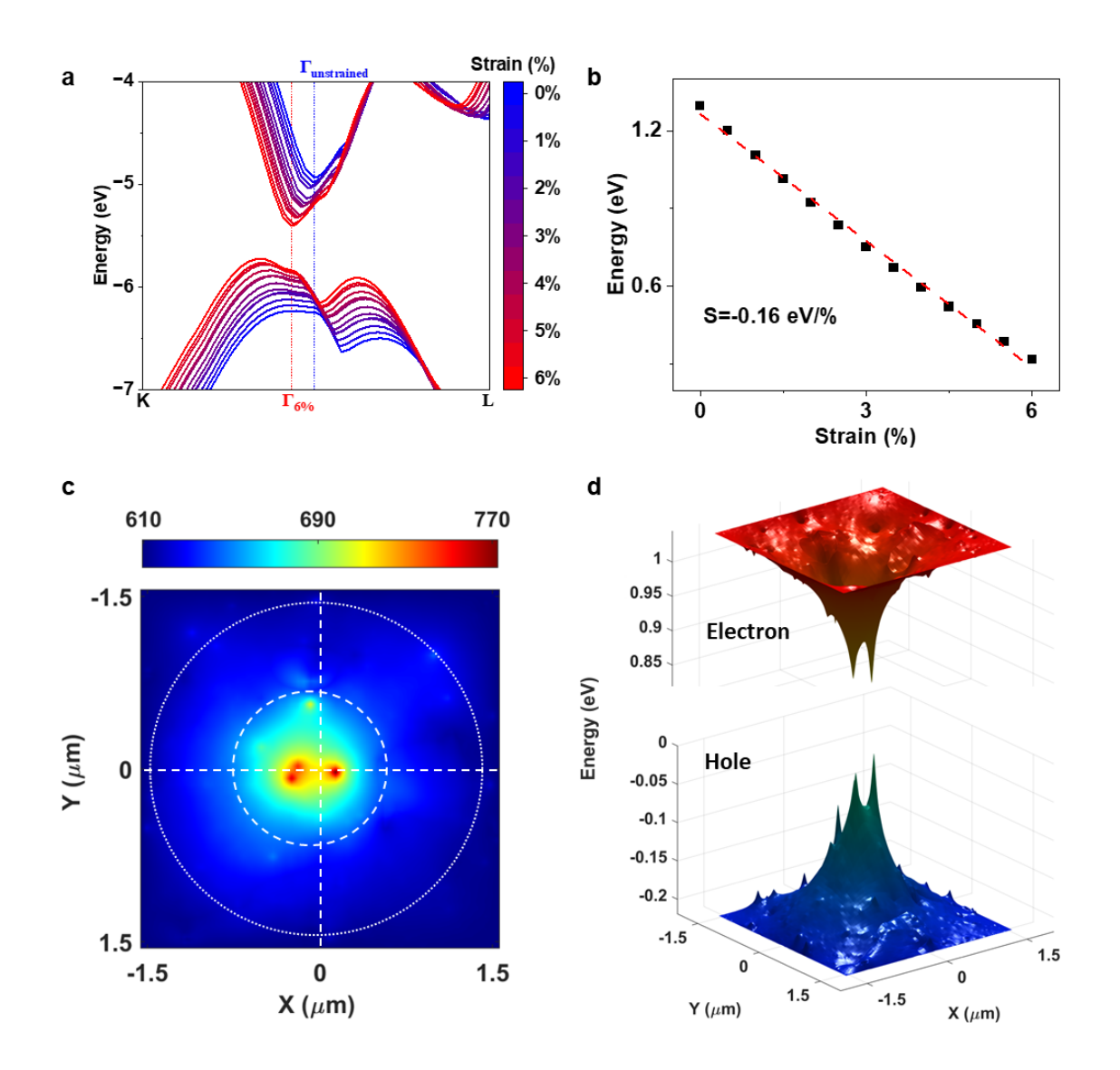


Figure 4. Biaxial tensile strain-modulated redshift of bandgaps. (a) DFT calculated band structures under different biaxial tensile strains from 0% to 6%. (b) Simulated redshift of bandgap (eV) as a function of biaxial tensile strain (%). (c) Correlation of the simulated bandgap converted into wavelength (nm) with the calculated strain distribution map shown in Figure 2(d). Dashed lines are guides to the eye. (d) Correlation of the simulated electron (CBM) and hole (VBM) energy profiles with the calculated strain distribution map shown in Figure 2(d).

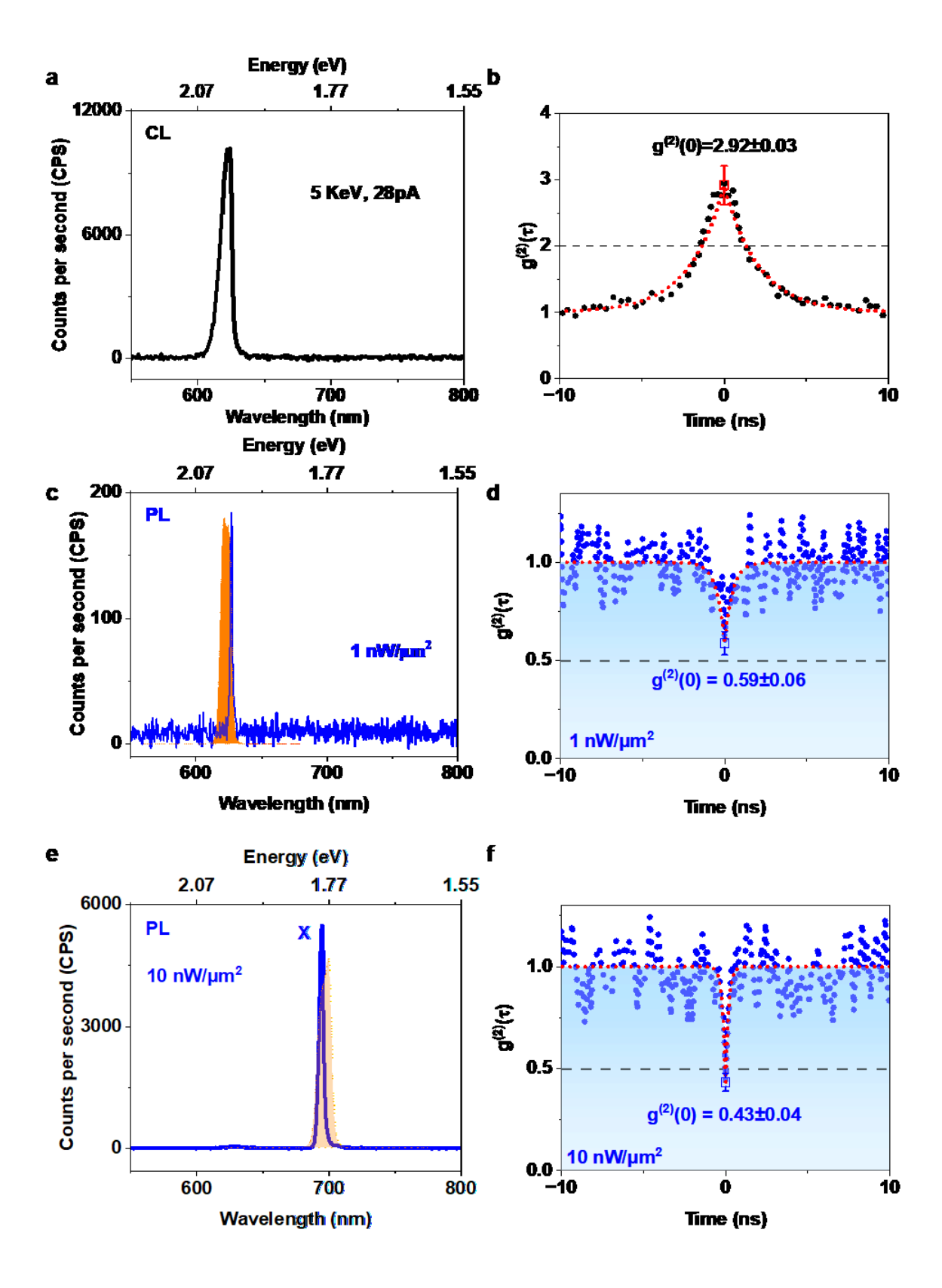


Figure 5. Comparison of the CL (at 9K) and PL (at 3.5K) photon statistics of emitters at pillar A. (a) A representative CL spectrum measured on tent A at T = 9 K, with an incident electron beam energy of 5 keV and a beam current of 28 pA. (b) Photon bunching measured for the 627 nm emitter in (a) acquired without a bandpass filter. The fitted second-order correlation function shows  $g^2(0)=2.92\pm0.03$ . (c) A PL spectrum collected on tent A at T = 3.5 K and with an incident laser power density of 1 nW/ $\mu$ m<sup>2</sup>. The orange shaded area indicates the spectral window of the narrow bandpass filter for photon antibunching measurements. (d) Photon-antibunching measured for this 627 nm emitter acquired using a narrow bandpass filter (625 nm, FWHM) = 10 nm. The fitted second-order correlation function shows  $g^2(0)=0.59\pm0.06$ . (e) Another PL spectrum measured on tent A at T = 3.5 K and with an incident laser power density of 10 nW/ $\mu$ m<sup>2</sup>. tThe orange shaded area indicates the spectral window of the narrow bandpass filter for photon antibunching measurements. (f) Photon-antibunching measured for the 694 nm SPE in (e) acquired using a narrow bandpass filter (697 nm, FWHM = 10 nm). The fitted second-order correlation function shows  $g^2(0)=0.43\pm0.04$ .